Balloon-borne observations of acoustic-gravity waves from the 2022 Hunga Tonga eruption in the stratosphere

Aurélien Podglajen[1,1], Alexis Le Pichon[2,2], Raphael F. Garcia[3,3], Solène Gerier[4,4], Christophe Millet[5,5], Kristopher M. Bedka[6,6], Konstantin V. Khlopenkov[7,7], Sergey M. Khaykin[8,8], and Albert Hertzog[9,9]

[1]Laboratoire de météorologie dynamique, Ecole Polytechnique
[2]CEA, DAM, DIF
[3]Institut Supérieur de l'Aéronautique et de l'Espace, ISAE-SUPAERO
[4]ISAE-SUPAERO
[5]CEA
[6]NASA Langley Research Center
[7]Science Systems and Applications
[8]CNRS-LATMOS
[9]Laboratoire de Météorologie Dynamique

November 30, 2022

Abstract

The 15 January 2022 explosion of the Hunga Tonga-Hunga Ha'apai (HT-HH) volcano generated an extreme, quasi-instantaneous perturbation of the atmosphere. As part of its adjustment following the eruption, a rich spectrum of waves radiated away from HT-HH and achieved worldwide propagation. Among numerous platforms monitoring the event, two long-duration stratospheric balloons flying over the tropical Pacific provided unique observations of Lamb and infrasonic wave arrivals, detecting three revolutions of the Lamb wave and five of infrasound waves. Combined with ground measurements from the infrasound network of the International Monitoring System, such observations bring precious insights into the eruption process (chronology and altitude of energy release), and highlight previously unobserved long-range propagation of infrasound modes triggered by the eruption and their dispersion patterns. A comparison between ground- and balloon-based measurements emphasizes generally larger signal-to-noise ratios onboard the balloons and further demonstrates their potential for infrasound studies.

Stratospheric balloon observations of infrasound waves from the January 15 2022 Hunga eruption, Tonga

Aurélien Podglajen[1], Alexis Le Pichon[2], Raphaël F. Garcia[3], Solène Gérier[3], Christophe Millet[2], Kristopher Bedka[4], Konstantin Khlopenkov[5], Sergey Khaykin[6], Albert Hertzog[7]

[1]Laboratoire de Météorologie Dynamique (LMD/IPSL), École polytechnique, Institut polytechnique de Paris, Sorbonne Université, École normale supérieure, PSL Research University, CNRS, Paris, France
[2]CEA, DAM, DIF, 91297 Arpajon, France
[3]Institut Supérieur de l'Aéronautique et de l'Espace (ISAE-SUPAERO), Université de Toulouse, 10 Ave E. Belin 31400 Toulouse, France
[4]NASA Langley Research Center, Hampton, Virginia, USA
[5]Science Systems and Applications, Inc., Hampton, Virginia, USA
[6]Laboratoire Atmosphères, Observations Spatiales (LATMOS), UVSQ, Sorbonne Université, CNRS, IPSL, Guyancourt, France
[7]Laboratoire de Météorologie Dynamique (LMD/IPSL), Sorbonne Universit, École polytechnique, Institut polytechnique de Paris, École normale supérieure, PSL Research University, CNRS, Paris, France

Key Points:

- Comparison between balloon-borne and ground-based observations of infrasound waves triggered by the January 2022 Hunga eruption
- Eruption sequence from infrasound in broad agreement with plume top height evolution
- Benchmark for long-range monitoring of infrasound from large explosive sources using stratospheric balloon observations

Corresponding author: Aurélien Podglajen, aurelien.podglajen@lmd.ipsl.fr

Abstract

The 15 January 2022 eruption of the Hunga volcano (Tonga) generated a rich spectrum of waves, some of which achieved global propagation. Among numerous platforms monitoring the event, two stratospheric balloons flying over the tropical Pacific provided unique observations of infrasonic wave arrivals, detecting five complete revolutions. Combined with ground measurements from the infrasound network of the International Monitoring System, balloon-borne observations may provide additional constraint on the scenario of the eruption, as suggested by the correlation between bursts of acoustic wave emission and peaks of maximum volcanic plume top height. Balloon records also highlight previously unobserved long-range propagation of infrasound modes and their dispersion patterns. A comparison between ground- and balloon-based measurements emphasizes superior signal-to-noise ratios onboard the balloons and further demonstrates their potential for infrasound studies.

Plain Language Summary

The eruption of the Hunga volcano on January 15 2022 was one of the most powerful blasts of the last century. This fast and strong perturbation of the atmosphere triggered atmospheric waves which were followed around the world multiple times. Here, we use records of sound waves emitted by the eruption from two balloons flying at about 20 km altitude over the Pacific combined with ground stations around the volcano to help characterize the event and its scenario. Due to weak relative wind and turbulence, the sounds on the balloon are generally clearer than on the ground, demonstrating the potential of high-altitude measurements for extreme events.

1 Introduction

While the 2021-2022 eruptive phase of Hunga volcano (Tonga) started in mid-December 2021, the paroxysmal explosion occurred on January 15^{th} 2022 around 04:16 UTC (Poli & Shapiro, 2022). Over the next hour, the volcanic plume penetrated deep into the atmosphere, reaching the stratopause and beyond (up to 58 km), whereas the umbrella cloud spread at approximately 35 km to form a 600 km diameter disk (Carr et al., 2022; Proud et al., 2022). The altitude of volcanic overshoots, the height and extent of the umbrella cloud set a new record for volcanic eruptions over the satellite era, overtaking Mount Pinatubo and its maximum reported plume height of 40 km (Holasek et al., 1996). The plume generated a large perturbation of the stratospheric aerosol layer and stratospheric composition (Millán et al., 2022), with likely substantial radiative impacts (Sellitto et al., 2022).

Besides triggering globally detected surface seismic waves (Poli & Shapiro, 2022) and tsunamis in several oceanic basins (Yuen et al., 2022; Matoza et al., 2022), the Hunga eruption also excited a wide spectrum of atmospheric waves, which were observed radiating away from the volcano (Matoza et al., 2022). These include the edge Lamb wave (Matoza et al., 2022; Wright et al., 2022), internal gravity waves (Wright et al., 2022; Ern et al., 2022) and infrasound (Matoza et al., 2022; Vergoz et al., 2022). The Lamb wave amplitude ($>$ 11 hPa peak-to-peak near Hunga) and propagation pattern are in particular reminiscent of the wave trains observed following the historical 1883 Krakatoa eruption (Matoza et al., 2022).

Most observations of Hunga waves were obtained by remote-sensing instruments or surface (micro)barometers, whereas the plume extended above stratospheric altitudes. In this paper, we present unique measurements of infrasound wave trains recorded in the stratosphere onboard two long-duration balloons flying over the Pacific. While balloon-borne instruments also detected acoustic signals corresponding to the early eruptive sequence of Hunga, including the January 13 explosion, the present study focuses on analyzing the waves triggered by the main eruption on January 15. We describe the first and multiple-revolution wave arrivals in balloon data and compare them to ground-based observations. Then, we discuss how infrasound may provide additional information on the eruption chronology and the value of ballon-borne measurements for this and similar events.

2 Data and Methods

2.1 Strateole-2 balloon data

In the frame of the Strateole-2 project (Haase et al., 2018), 17 superpressure balloons (SPBs) were launched from Seychelles by the French space agency (CNES) in October-December 2021. Strateole-2 SPBs are constant-volume balloons designed to fly several months at a chosen density level in the tropical upper troposphere-lower stratosphere (between 18.5 and 21 km) . On January 15 2022, two SPBs (STR1 and TTL4) remained over the tropical Pacific at about 19 km above sea level. Their altitudes and approximate locations are given in Table 1 and displayed in Fig. 1 a); both balloons drifted horizontally following the wind, which for infrasound implies neglegible Doppler shift but changes the distance to source with time.

Among various instruments, all Strateole-2 payloads notably include the TSEN temperature and pressure sensors (Hertzog et al., 2007) and a GPS. Position is measured every 30 s with 1 m vertical resolution. The pressure sensor (Paroscientific-6000-15A) samples at 1 Hz with 100 mPa resolution. It has a flat frequency response over the range of interest (up to 0.25 Hz).

SPBs undergo vertical oscillations forced by atmospheric motions and modulated by the balloon's response (Massman, 1978; Vincent & Hertzog, 2014). Due to the background vertical pressure gradient, such vertical motions induce additional apparent pressure fluctuations compared to measurements obtained at constant altitude. To correct for this effect, we remove the component of pressure fluctuations due to the hydrostatic pressure gradient to derive the Eulerian (constant-altitude) pressure perturbation p:

$$p = p_l \exp\left(\frac{g}{R_d T}\zeta'\right) - \overline{p} \qquad (1)$$

where p_l and T are the raw (balloon-following) pressure and temperature, $\overline{p}_l$ the time-averaged pressure, ζ' geopotential height anomalies, $g = 9.81\ \mathrm{m\,s^{-2}}$ and $R_d = 287$ J/K/kg. GPS position is interpolated at 1 s to compute ζ' and p. The effect of correction 1, described in Supplement S1, is significant at frequencies around that of the balloon oscillations ($\sim$4.5 mHz) or lower, but for infrasound frequencies above $\sim$0.02 Hz, p closely follows p_l. The precision of the pressure data is sufficient to detect the energy peak of the oceanic microbarom around 0.2 Hz (Bowman & Lees, 2018).

2.2 IMS microbarometer data

Infrasound stations from the International Monitoring System (IMS) of the Comprehensive Nuclear-Test-Ban Treaty Organization are arrays of microbarometers sensitive to acoustic pressure variations between 0.02 and 4 Hz with a flat frequency response (e.g., Hupe et al., 2022). We use data from 5 stations listed in Table 1 and located either in the vicinity of the balloons or at distances of 1,800-4,000 km from Hunga (Fig. 1 a). A thorough investigation of Hunga infrasound waves in IMS data is presented in Vergoz et al. (2022).

2.3 Ancillary dataset: geostationary satellite data

We also employ stereoscopic 10-minute-resolution cloud top height retrievals to infer the chronology of the eruption. These data are derived at NASA Langley using the

Table 1. Receiver coordinates and infrasound properties in ground-based and balloon-based records.

receiver	distance (km)	Latitude °N	Longitude °E	altitude (km)	c_g (m/s)	Observed T_L (30-40 mHz) with respect to IS22 (dB) WP1	WP2	WP3
IS07	5227	-19.93	134.33	ground	297.00	-15.66	-14.04	-37.19
IS22	1849	-22.18	166.85	ground	297.00	0.00	0.00	0.00
IS24	2755	-17.75	-149.30	ground	261.00	-28.27	ND	ND
IS36	2699	-43.92	176.48	ground	300.00	-15.82	-16.02	-28.11
IS40	3957	-4.10	152.10	ground	301.00	-22.72	-15.89	-28.67
IS57	8645	33.61	-116.45	ground	292.00	-35.72	-23.67	-33.18
STR1	2238	-0.80	-171.64	20.5	279.00	-14.89	-12.68	-24.75
TTL4	7640	15.70	-116.02	18.5	276.00	-26.41	-22.75	-36.62

ND: Wavepacket not discernible at receiver.

parallax between almost-synchronized 10.3 μm-band brightness temperature images obtained from different viewing angles by the geostationary satellites GOES-17 (Eastern Pacific sector) and Himawari-8 (Western Pacific sector). For the Hunga plume, the spatial resolution of the product is about 6 km and its vertical accuracy typically lies between 0.2-0.4 km. Further description of the retrieval method is provided in Supplement S2.

2.4 Numerical simulations of infrasound attenuation

In a horizontally isotropic medium, the modulus $|P|$ (ducted) wave pressure amplitude varies along propagation path due to geometric spreading, following (e.g., Pierce & Posey, 1971):

$$|P|(d,z) = \sqrt{\frac{\rho}{\rho_r}\frac{\sin(d_r/a)}{\sin(d/a)}}|\tilde{P}|(z) \tag{2}$$

where a is the Earth radius, d the horizontal distance (range) from Hunga (d_r an arbitrary reference distance), ρ the density, ρ_r a reference density ($\rho_r = 1.2$ kg/m^3 except if stated otherwise) and the density- and range-scaled pressure amplitude $|\tilde{P}|$ a priori depends only on altitude z. Note that this vertical scaling only retains the density factor in sonic impedance $I = \rho c$, since variations of the sound speed factor c are overshadowed by the vertical structure of the mode for long-range horizontal propagation. Equation 2 also neglects leakage and absorption. Most importantly, the assumed isotropic propagation breaks for infrasound waves which are sensitive to the stratospheric wind fields (Matoza et al., 2022; Vergoz et al., 2022).

To apprehend expected infrasound amplitude evolution for different azimuths, we compute (linear) attenuation at a given frequency using the range-dependent parabolic equation (PE) solver NCPA-ePape(Waxler et al., 2021). The model assumes planar propagation along the orthodromes and the influence of wind is encapsulated into an effective sound celerity c_{eff}. c_{eff} sections along each great-circle path are defined by:

$$c_{\text{eff}}(d,z) = \sqrt{\gamma R_d T(d,z)} + \mathbf{u_h}(d,z)\cdot\mathbf{e_x}(d,z), \tag{3}$$

with γ the capacity ratio, T the temperature, $\mathbf{u_h}$ the horizontal wind vector and $\mathbf{e_x}$ the range-dependent unit vector pointing from the source towards the receiver. c_{eff} profiles, calculated from the European Center for Medium-range Weather Forecast (ECMWF) ERA5 reanalysis (Hersbach et al., 2020), are shown in Fig. 1 b). Above 60 km and up to 140 km, ECMWF profiles are merged with temperature and wind climatologies (MSISE00 and HWM14, Picone et al., 2002; Drob et al., 2015) perturbed by a range-dependent realization of a gravity-wave field prescribed following Gardner et al. (1993). For the lower boundary condition, we assume a rigid ground (infinite impedance). T_L transmission losses (T_L) between Hunga and the sensors are quantified in dB, i.e.:

$$T_L(d,z) = 20\,\log_{10}\left(\frac{|P|(d,z)}{|P|(d=d_r, z=z_r)}\right) \tag{4}$$

where z and z_r are the receiver and reference altitude. Figure 1 c), d), e) presents sections of scaled transmission loss $\tilde{T}_L$ (calculated using Eq. 4 and scaled pressure $|\tilde{P}|$) and curves of regular T_L from NCPA-ePape. Results highlight expected anisotropic propagation. In the spirit of comparing signal-to-noise ratios (SNR) onboard balloons and on the ground, keeping the $\rho^{-\frac{1}{2}}$ factor has its merits, since possible sources of dynamical noise at high altitude (i.e., balloon or gondola wake encounters) scale with density and dominate over altitude-independent electronic noise (Krishnamoorthy et al., 2020a).

Note that, as stressed by Matoza et al. (2022), directly interpreting Hunga infrasound attenuation quantitatively using PE is difficult due to various uncertainties arising in this peculiar case, including a complex source, possible invalidity of the underlying approximations discussed in Waxler and Assink (2019) and biases in wind field from climatology, gravity-wave perturbation or even reanalysis (e.g. Podglajen et al., 2014). Hence, PE simulations are only used here as a pedagogical tool to contextualize differences between receivers.

3 Results

3.1 First infrasound arrivals

Pressure spectrograms during the first overpass of the waves (Fig. 2) show arriving first the low-frequency Lamb wave pulse (Matoza et al., 2022; Vergoz et al., 2022; Wright et al., 2022) extending up to ~ 3 mHz. Above $\sim$10 mHz, instead of a single dominant pulse several receivers (e.g., IS22, STR1, Fig. 2) recorded a complex infrasound arrival sequence within which one may identify at least three distinct initial wavepackets (WPs) peaking around 20-30 mHz. WPs onsets, separated by periods of reduced acoustic power, are highlighted in Fig 2. The delay between WP1&3 is without ambiguity beyond the spread in arrival times which can be expected for acoustic wave generated by a unique trigger. As for WP1&2, the roughly constant time separation observed among receivers at different short-range distances and azimuths from Hunga (IS22, STR1), together with the absence of similar duplication of WP3, rules out differential propagation. Overall, this suggests that the WPs originate from successive source-level events. Dispersion, however, manifests itself at larger distances, creating longer, duplicated wavepackets at TTL4 (in particular WP3).

Taking advantage of the reproducible and highly structured arrival sequence, we deduced approximate average travel speed c_g for the different sensors, as explained in Supplement S2. c_g values (Table 1) vary consistently with prevailing stratospheric wind conditions (weakest to the East of the volcano, strongest to the West). Back-propagating WPs to the source suggests pulses of emission around 04:15, 04:53 and 08:27 ($\pm$ 5 minutes). This chronology will be further discussed in Sect. 4.1.

10-minute-averaged spectra at the arrival of WP1 (Fig. 2 a, b) show a significant enhancement over the whole acoustic range compared to the period immediately prior to it, with a peak around 20-30 mHz, especially striking for balloon sensors. WP2 has somewhat higher frequency, peaking around 30-40 mHz in balloon records.

Besides distinct WPs, balloon observations exhibit a lasting tail of enhanced acoustic variability above 0.01 Hz with a return to pre-eruption levels after about a day. This feature is akin to the Coda observed in seismic waves (e.g. Aki, 1997) and likely results

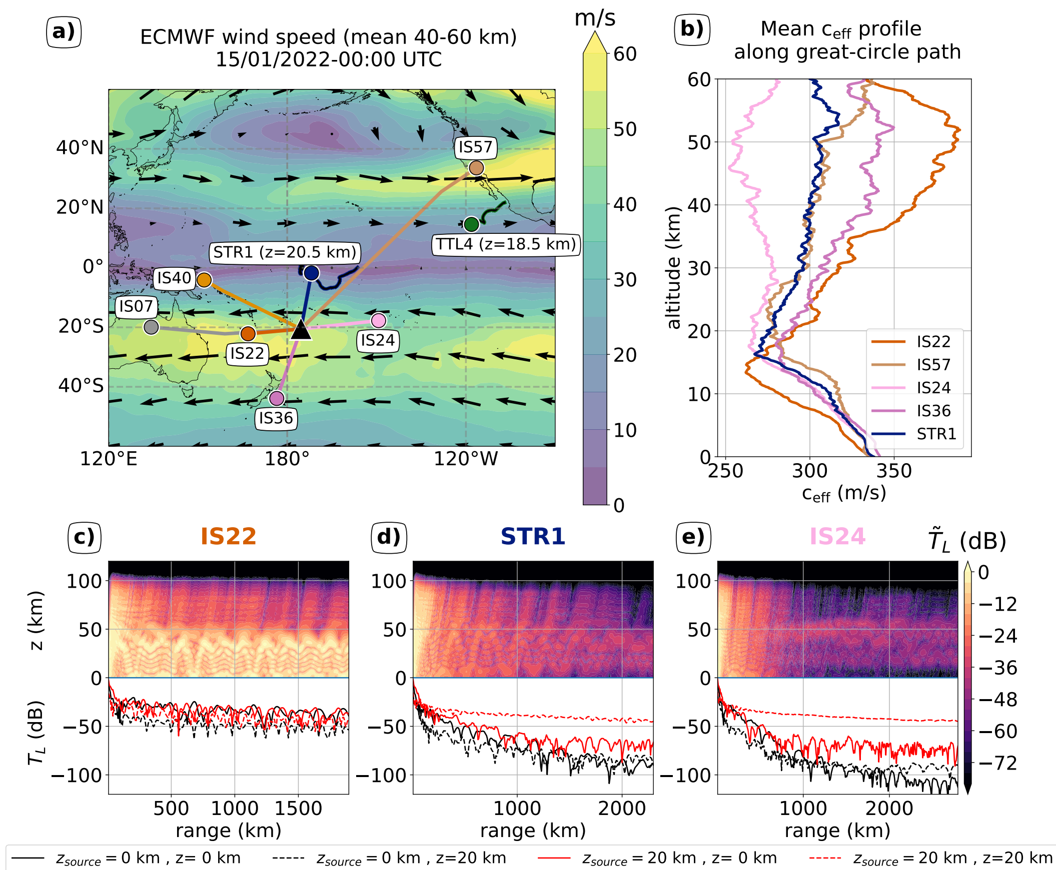

Figure 1. (a) Upper-stratospheric (40-60 km average) horizontal wind direction (vectors) and speed (contours) on January 15 2022 from ECMWF. Colored dots represent the location of the ground stations and balloons at the time of the main blast, with (colored lines) Hunga-to-receiver orthodromes. Balloon trajectories from the eruption until the termination of the flights are shown in black. (b) Average effective sound speed profile along selected orthodromes in (a). Panels (c), (d), (e) (top) Along-path sections of scaled transmission loss $\tilde{T}_L$ with respect to $d_r = 17.5$ km, $z_r = z_{source}$f in the directions of IS22, STR1 and IS21 computed for a ground source of frequency 0.05 Hz. (Bottom) Transmission loss profiles T_L at the ground (solid lines) and 20 km a.s.l. (dashed lines) for a point source at the ground (black) and 20 km (red).

from multipathing and wave scattering by small-scale inhomogeneities, e.g. pre-existing gravity waves (Chunchuzov et al., 2011).

3.2 Anisotropy of infrasound propagation

A large spread in infrasound-signal amplitude is found among receivers, as summarized in Table 1, which reports observed transmission losses with respect to IS22 for the 3 WPs. This results from the variability of along-path stratospheric winds near Hunga (Fig. 1 (a)), which imply large variations in the associated c_{eff} profiles (Fig. 1 (b)) and infrasound ducting efficiency.

To illustrate this, selected T_L sections, estimated with ePape for a ground source of frequency 0.05 Hz, are displayed in Fig. 1. Towards IS22, strong tailwinds support a stratospheric duct from $\sim$ 50 km down to the ground (Fig 1 c), explaining low attenuations for receivers West of the volcano (IS07, IS36, IS40). In other directions (STR1, IS24), head- and crosswinds hamper propagation at the surface. Nevertheless, a shallower duct exists, tied to the temperature minimum around the tropopause and confined to the upper troposphere-lower stratosphere (UTLS). We will refer to it as the UTLS duct. This duct generates larger scaled amplitudes $|\tilde{P}|$ at stratospheric balloon flight altitude (Fig 1 d, e).

Despite the qualitative agreement with Table 1 for each WP taken separately, this reasoning does not explain the observed increase in IS22-relative attenuations from WP1 to WP3. As reported by Matoza et al. (2022), the scatter in T_L is also smaller than in PE simulations forced at ground level. Besides dispersion, model biases and violated assumptions (e.g., linearity), these discrepancies likely partly arise due to the complexity of the time-varying source (Matoza et al., 2022). While a detailed assessment is beyond the scope of our study, we note that a possible (but not sole) contributing factor may be the event-dependent vertical distribution of the forcing. Indeed, Figure 1 suggests that significant generation at upper levels (here 20 km) tends to reduce anisotropy compared to lower-level sources.

3.3 Multiple revolutions of acoustic waves

Longer recordings over the days following the eruption reveal successive revolutions of infrasound waves (Vergoz et al., 2022), as shown for the balloons and nearby stations IS22 and IS57 in Fig. 3. In the following, we adopt the convention for multiple passages of Matoza et al. (2022); Vergoz et al. (2022): A1 for the direct (short-orthodrome) arrival, A2 for the first antipodal arrival, A3 for A1 + one revolution etc. Ground measurements are polluted by sporadic bursts of noise related to atmospheric turbulences, which prevent detections under high surface-wind conditions beyond A1 (Vergoz et al., 2022). A clearer picture emerges from balloon observations (Fig. 3 (b), (d)), which almost exclusively exhibit geophysical signals above 30 mHz, and record clear arrivals up to A10 at STR1.

Figure 3 e-n highlights distinct acoustic dispersion patterns in Fig. a-d, which are described in the following. Although dispersion mixes A2 and A3 at STR1 (Fig. 3 e), one can clearly distinguish an A2 wavetrain with virtually no dispersion (”compact mode”) retaining the imprint of the source (i.e., distinct WP1 and WP2) over several revolutions. This mode has typical round-the-world-transit speed of 288 m/s ($\pm$1 m/s). It is visible only at STR1, at least for passages A2 and A4 (Fig. 3 f). On Fig. 3 e), second wavetrain (”dispersive modes”) follows. It is typically slower ($\sim$275 m/s), mixes with A3, and features two dispersion lines around 20 mHz and 70 mHz. A double dispersion line was also observed for A1 in Kenya ($d = 15,750$ km) (Vergoz et al., 2022). The 70 mHz dispersive mode is also evident in passages A2 and A4 at TTL4 (Fig. 3 g and i) but absent at IS57 (Fig. 3 l and n). The lower dispersion curve is longer-lived and appears at least at

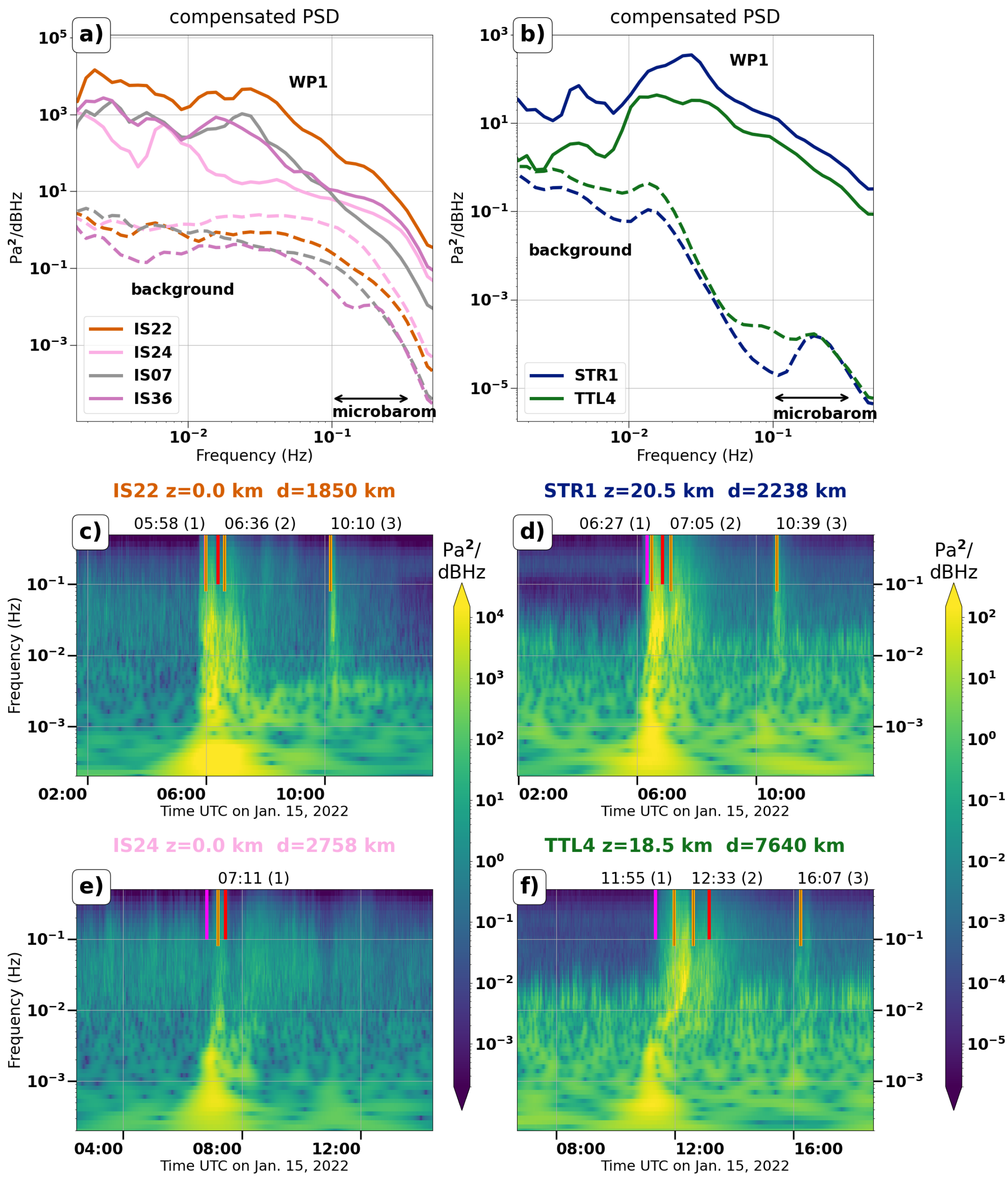

Figure 2. Compensated power spectral density (PSD multiplied by frequency) during the overpass of WP1 (solid line) and background of the 3 hours before the eruption (dashed line) for (a) the ground stations and (b) the balloons. c), d), e), f) Selected spectrograms of the pressure signals corresponding to the first wave arrivals. The orange vertical lines indicate arrival times of WPs (timings reported above). Purple and red lines correspond to expected arrival times for the first event (see text) assuming travel speeds $c_g = 300$m/s and $c_g = 240$m/s, respectively.

A2-4 at TTL4 and A2-10 at STR1, as well as at IS22 and IS57. From the spectrograms (Fig. 3 a)), we estimate $\frac{\partial c_g}{\partial \omega} \simeq -500\text{-}600$ m for this mode, for which the decrease in travel speed with frequency results in a flattening of the wave trains in frequency-time space over successive circumnavigations (Fig. 3 a)-d)). Finally, for completeness, a non-dispersive 30-mHz wavepacket was recorded for A3 at TTL4, although not at IS57 (Fig. 3 h-m).

The nature of this family of modes remains unclear. Their typical celerity resembles stratosphere-ducted infrasound with wind bringing substantial contribution in one or the other direction. Contrasted efficiency of wind ducting in different propagation directions likely plays a role in the favored "antipodal" propagation of the dispersive modes found at TTL4. It is noteworthy that, whereas ground stations IS22 measures larger amplitudes for A1, the situation reverses for later overpasses. For instance, the signal amplitude near the lower dispersion curve for passages A2 and A4 seems systematically larger at balloon altitude. Some arrivals clearly detected in the balloon signals are not discernible in ground recordings (e.g., at TTL4, the upper dispersion line for A2 and A4 or the A3 arrival). Altogether, this suggests that long-lived modes are ducted at upper levels, although their vertical structure and the role of wind in supporting them warrants further investigations.

4 Discussion

4.1 Infrasound emission and chronology of the eruption

In Sect. 3.1, we argued that STR1 and IS22 captured the same infrasound emission sequence. The inferred scenario is substantiated in Fig. 4, which depicts shifted time series of 3-minute 30-40 mHz-filtered (a) signal variance (proportional to acoustic power) and (b) scaled amplitude for selected receivers. High correlations with IS22 are seen for other shorter-range sensors at various distances West of Hunga (IS07, IS40, IS36). They benefit from limited dispersion effects, likely thanks to the source proximity and overall similar (and favorable) propagation conditions (Vergoz et al., 2022). In contrast, signals are less distinct East of Hunga (IS24). Interestingly, balloon STR1 exhibits the highest correlation with IS22 around WP1&2 and has similar scaled amplitude $|\tilde{P}|$.

Distinct WPs likely mirror different phases of acoustic-wave emission at the source. Vergoz et al. (2022) found that infrasound and seismic wave activity coincide for the early part of the eruption but decouple at later stages (i.e., WP 3). In very different eruptive contexts, previous studies (e.g., Fee et al., 2010) have found a correlation between radiated acoustic power and plume height. To explore this link with volcanic aerial activity, Figure 4 a) presents the evolution of maximum plume altitude from stereoscopic cloud top height (CTH) retrievals during the eruption. Notwithstanding a $\sim$20-minute delay between the onsets of infrasound WPs and observations of plumes reaching their ceiling, a rough match may be found between (i) WP1 and the first plume reaching the mesosphere (04:37), and (ii) WP3 and a later plume observed reaching 38 km at 08:47. The higher initial plume also seems associated with larger infrasound power (Fig. 4) and smaller anisotropy (Sect. 3.2) than the lower-height 08:47 injection. Contrary to WP1 and 3, tentative attribution of WP2 is not obvious. The second extended mesospheric intrusion occurs slightly West of Hunga and closely follows the first in time. CTH data also indicate a 48-km overshoot at Hunga's location at 05:17 which may better correspond. Event identification is challenging and not always meaningful given the complexity of the plume evolution and sources at play. Nevertheless, the general comparison tends to suggest a significant role of processes related to plume dynamics (Woulff & McGetchin, 1976; Matoza et al., 2009; Fee & Matoza, 2013; Watson et al., 2022) in Hunga infrasound generation. It highlights the value of STR1's records which, gathered inside a waveguide, appear well-placed for source characterization.

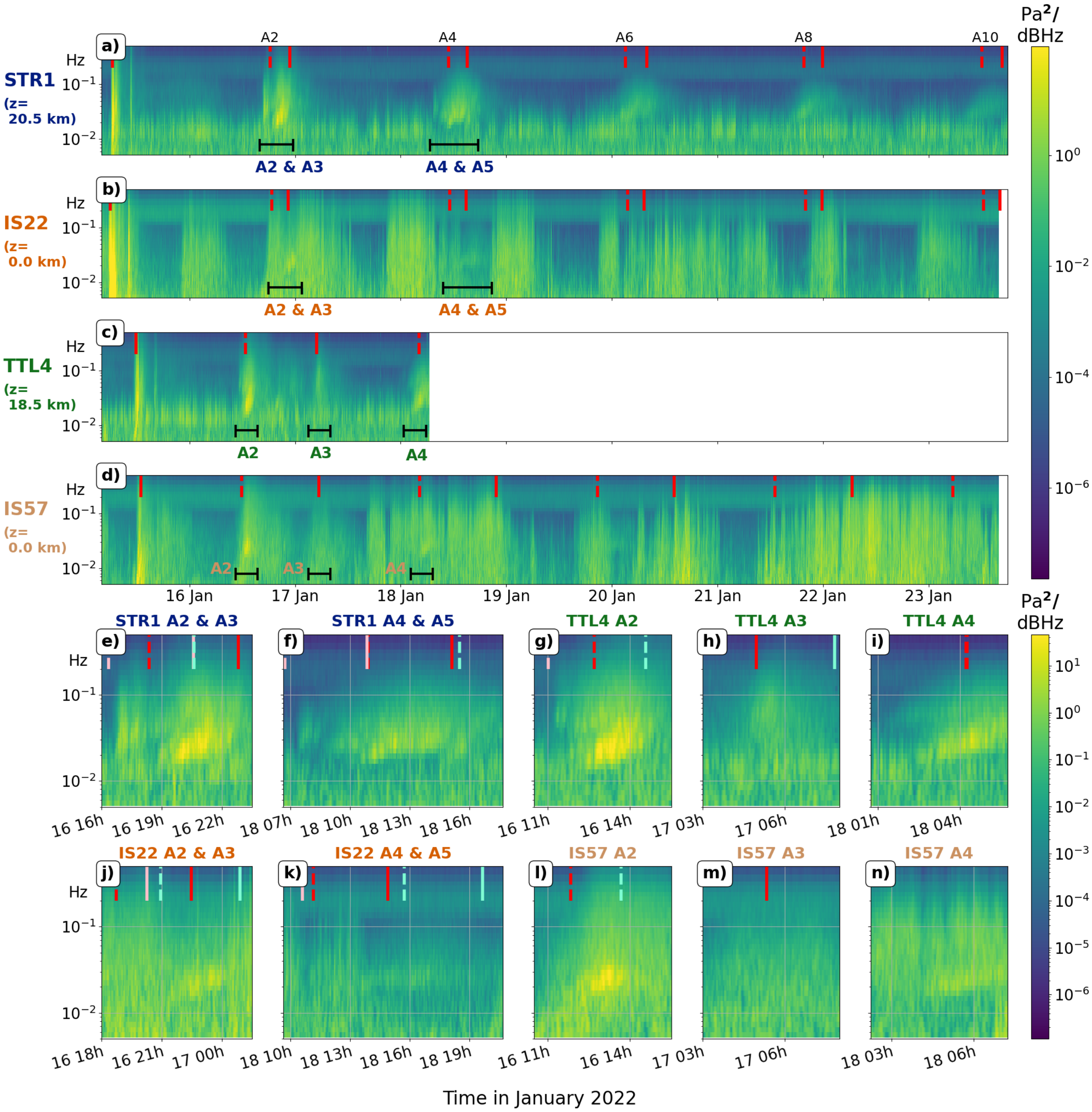

Figure 3. Spectrograms of the pressure signals at balloons a) STR1 and c) TTL4 and ground stations b) IS22 and d) IS57. Expected arrival times are shown for the 275 (red) m/s travel speed (solid lines for "direct", dashed for antipodal). TTL4 time series stop on January 18 due to its burst. e) to n) Zoom on the (e, g, j, l) first antipodal arrival and (e, h, m) second direct and (f, i) antipodal arrivals at (e to i) the balloons and (j to n) ground stations. Direct and antipodal arrivals superpose partly at STR1 and IS22. Further expected arrival times for 290 (pink) and 260 (light green) m/s are displayed.

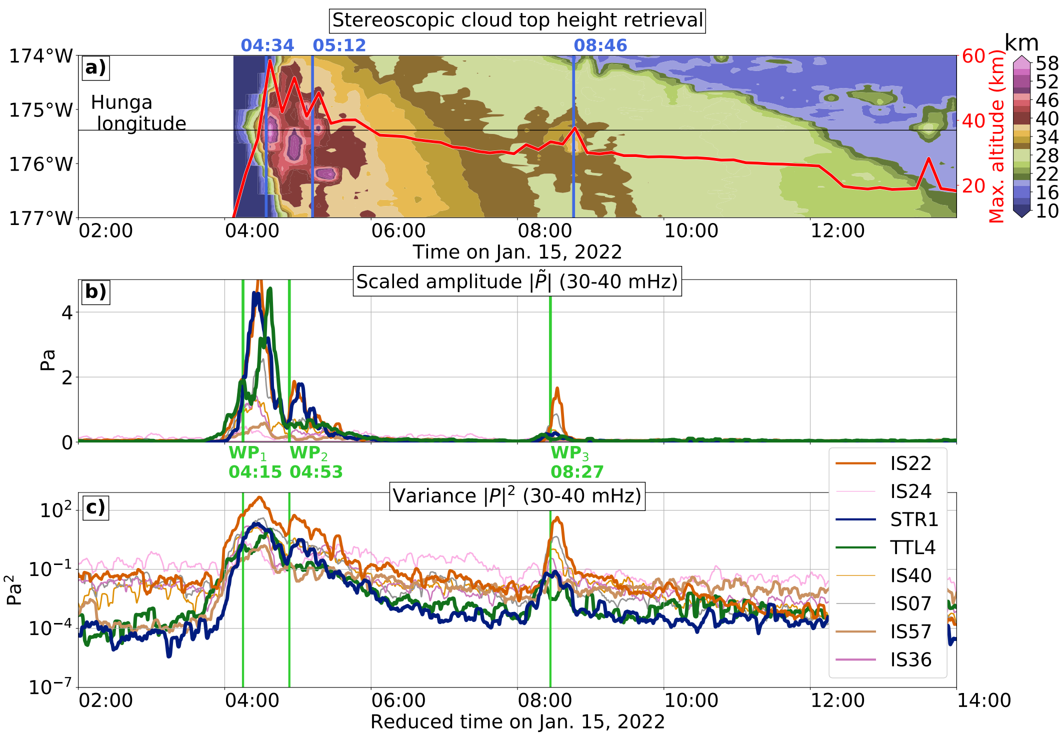

Figure 4. (a) Hovmöller diagram of plume top altitude and (red line) time series of maximum plume height in the area (20.75°S-20.35°S, 175.7°W-175.3°W). (b) 3-minute scaled pressure amplitude $|\tilde{P}|$ time series (30-40 mHz filtered) for selected receivers. The reference in Eq. 2 is here chosen at STR1 ($\rho_r = 0.08$ kg/m^3, $d_r = 2,210$ km). (c) 3-minute $|P|$ variance (30-40 mHz). Green vertical lines are time onsets of WPs, and blue ones are the same shifted by 19 minutes. The time axis represents range-corrected reduced time $t_r = t - \frac{d}{c_g}$, c_g from Table 1.

The presented scenario of intermittent aerial activity is generally consistent with other atmospheric records of the event (e.g., Astafyeva et al., 2022; Vergoz et al., 2022; Wright et al., 2022). For example, ground pressure measurements at Nukua'lofa (Tonga, $d = 64$ km) show 4 major pressure minima (Wright et al., 2022), 3 of which closely match our WPs (04:36, 05:10 and 08:46). However, no enhanced infrasound corresponds to the third minimum ($\sim$ 05:51).

4.2 Advantages and potential limitations of balloon measurements

Our study evidences an infrasound signal-to-noise ratio (SNR) improved by a factor of at least 10 at lower stratospheric altitudes compared to the ground (Fig. 2 a, b and 4). Reasons include (1) the location of the receiver inside the UTLS waveguide and (2) reduced noise in the absence of wind relative to the sensor (Bowman & Lees, 2015; Bowman & Krishnamoorthy, 2021; Krishnamoorthy et al., 2020b).

For a ground source, infrasound signals are larger at the surface in conditions supporting deep propagation (West of Hunga). However, upper-air reception appears favored in otherwise unfavorable propagation conditions (IS21, Fig. 1 (e)). In general, the strong anisotropy observed for ground receivers is mitigated at UTLS levels, an advantage reinforced for sources around the UTLS duct (Fig. 1 (e)). It is exacerbated in the case of Hunga for long-range paths from multiple circumnavigations, for which larger signals are encountered in the stratosphere.

Ground-level winds exceeding a few m/s (Vergoz et al., 2022) typically result in a background noise level ($|P|^2$) about 3 orders of magnitude larger at IMS stations than recorded onboard the balloons, as shown in Fig. 4). Turbulence-induced noise is a well-known challenge of ground-based infrasound monitoring (e.g., Marty, 2019). Under low surface winds, reduced noise at the ground may be associated with better SNR there, as detailed in Supplement S4.

Despite its assets, the balloon platform might suffer from specific biases. One is related to the balloons oscillations (Massman, 1978), which are only partially corrected by the current implementation of Eq. 1 (see Supplement S1 for further discussion). Others may be unanticipated. For instance, Garcia et al. (2022) recently identified a mismatch between balloon observations and pressure fluctuations expected from large-incidence infrasound generated by seismic waves. Those authors ruled out resonant excitation of pendulum oscillations and proposed that the observed discrepancies are induced by movements of the balloon/gondola system. For Hunga infrasound, we argue that the repeated recordings of continuous dispersion curves in the infrasound range between 10 and 100 mHz (Fig. 3) advocate against large artifacts related to resonance at specific frequencies, demonstrating that pressure measurements onboard balloons are quantitatively reliable for shallow-incident-angle infrasound waves.

5 Conclusions

The cataclysmic January 15 2022 eruption of the Hunga volcano triggered a wide spectrum of atmospheric waves unprecedented in modern observational records. Located 2,200 and 7,800 km away from the volcano, two long-duration stratospheric balloons measured a clear signature of the surface-guided Lamb wave and of infrasound waves. Supported by plume top height data, the first arrival of infrasound wave packets at frequencies between 0.02 and 0.05 Hz indicate several bursts of acoustic wave emission highlighting a complex eruption scenario. Later infrasound arrivals associated with multiple revolutions (up to A10) could be detected until the end of the flights, 9 days after the eruption, corresponding to wavepackets circumnavigating the globe 5 times.

Together with balloon-borne infrasound earthquake (Brissaud et al., 2021; Garcia et al., 2022), surface (Bowman & Albert, 2018; Young et al., 2018) and underground (Bowman & Krishnamoorthy, 2021) explosion detections, this exceptionally long-range detection of acoustic waves from the Hunga eruption demonstrates the potential of long-duration stratospheric balloons for the monitoring of natural and anthropogenic hazards. Shortcomings of the 2021 Strateole-2 infrasound payload are (1) the limited time resolution of pressure measurements (1 Hz) and (2) the lack of azimuth and incidence angle measurements. The former will be improved in future campaigns by increasing the sampling rate of pressure measurements. For the latter, different teams recently tried to cover the gap with IMUs (Garcia et al., 2020; Bowman et al., 2022) or antennas of pressure sensors (Krishnamoorthy et al., 2019; Garcia et al., 2020). We recommend including such dedicated instumentation in the future to provide additional constraint on wave properties. Finally, the response of SPBs to high-frequency atmospheric excitations is prone to significant uncertainties (Podglajen et al., 2016; Garcia et al., 2022). Further theoretical investigations are warranted to improve inferences on atmospheric wave properties from this invaluable platform (Bowman et al., 2022).

6 Open Research

Strateole-2 data is available at `https://data.ipsl.fr/catalog/strateole2/eng/catalog.search#/search?from=1&to=30`. IMS data is available upon request at `https://www.ctbto.org/specials/vdec` (last accessed on 2022-05-11). ECMWF data can be found at `https://cds.climate.copernicus.eu/cdsapp#!/dataset/reanalysis-era5-pressure-levels?tab=form` (last accessed on 2022-05-11). GOES-17 and Himawari-8 datasets are publicly accessible through Amazon Web Services (AWS). AWS Open Data description pages: `https://registry.opendata.aws/noaa-goes/` and `https://registry.opendata.aws/noaa-himawari/`.

Acknowledgments

The authors thank Daniel Bowman, David Fee and Alex Iezzi for insightful reviews, and Alain Hauchecorne and François Lott for discussions. The sponsorship of CNES, CNRS-INSU and NSF to Strateole-2 balloon activities is gratefully acknowledged.

References

Aki, K. (1997). Seismic Coda Waves: A Stochastic Process in Earth's Lithosphere. In S. A. Molchanov & W. A. Woyczynski (Eds.), *Stochastic Models in Geosystems* (pp. 1–24). New York, NY: Springer. doi: 10.1007/978-1-4613-8500-4_1

Astafyeva, E., Maletckii, B., Mikesell, T. D., Munaibari, E., Ravanelli, M., Coisson, P., ... Rolland, L. (2022). The 15 January 2022 Hunga Tonga Eruption History as Inferred From Ionospheric Observations. *Geophysical Research Letters*, *49*(10), e2022GL098827. doi: 10.1029/2022GL098827

Bowman, D. C., & Albert, S. A. (2018, June). Acoustic event location and background noise characterization on a free flying infrasound sensor network in the stratosphere. *Geophysical Journal International*, *213*(3), 1524–1535. doi: 10.1093/gji/ggy069

Bowman, D. C., & Krishnamoorthy, S. (2021). Infrasound From a Buried Chemical Explosion Recorded on a Balloon in the Lower Stratosphere. *Geophysical Research Letters*, *48*(21), e2021GL094861. doi: 10.1029/2021GL094861

Bowman, D. C., & Lees, J. M. (2015). Infrasound in the middle stratosphere measured with a free-flying acoustic array. *Geophysical Research Letters*, *42*(22), 10,010–10,017. doi: 10.1002/2015GL066570

Bowman, D. C., & Lees, J. M. (2018). Upper Atmosphere Heating From Ocean-Generated Acoustic Wave Energy. *Geophysical Research Letters*, *45*(10), 5144–

5150. doi: 10.1029/2018GL077737

Bowman, D. C., Rouse, J. W., Krishnamoorthy, S., & Silber, E. A. (2022, May). Infrasound direction of arrival determination using a balloon-borne aeroseismometer. *JASA Express Letters*, *2*(5), 054001. doi: 10.1121/10.0010378

Brissaud, Q., Krishnamoorthy, S., Jackson, J. M., Bowman, D. C., Komjathy, A., Cutts, J. A., … Walsh, G. J. (2021). The First Detection of an Earthquake From a Balloon Using Its Acoustic Signature. *Geophysical Research Letters*, *48*(12), e2021GL093013. doi: 10.1029/2021GL093013

Carr, J. L., Horváth, Á., Wu, D. L., & Friberg, M. D. (2022). Stereo Plume Height and Motion Retrievals for the Record-Setting Hunga Tonga-Hunga Ha'apai Eruption of 15 January 2022. *Geophysical Research Letters*, *49*(9), e2022GL098131. doi: 10.1029/2022GL098131

Chunchuzov, I. P., Kulichkov, S. N., Popov, O. E., Waxler, R., & Assink, J. (2011, October). Infrasound scattering from atmospheric anisotropic inhomogeneities. *Izvestiya, Atmospheric and Oceanic Physics*, *47*(5), 540–557. doi: 10.1134/S0001433811050045

Drob, D. P., Emmert, J. T., Meriwether, J. W., Makela, J. J., Doornbos, E., Conde, M., … Klenzing, J. H. (2015). An update to the Horizontal Wind Model (HWM): The quiet time thermosphere. *Earth and Space Science*, *2*(7), 301–319. doi: 10.1002/2014EA000089

Ern, M., Hoffmann, L., Rhode, S., & Preusse, P. (2022). The mesoscale gravity wave response to the 2022 tonga volcanic eruption: Airs and mls satellite observations and source backtracing. *Geophysical Research Letters*, *49*(10), e2022GL098626. Retrieved from `https://agupubs.onlinelibrary.wiley.com/doi/abs/10.1029/2022GL098626` (e2022GL098626 2022GL098626) doi: https://doi.org/10.1029/2022GL098626

Fee, D., Garces, M., & Steffke, A. (2010, June). Infrasound from Tungurahua Volcano 2006–2008: Strombolian to Plinian eruptive activity. *Journal of Volcanology and Geothermal Research*, *193*(1), 67–81. doi: 10.1016/j.jvolgeores.2010.03.006

Fee, D., & Matoza, R. S. (2013, January). An overview of volcano infrasound: From hawaiian to plinian, local to global. *Journal of Volcanology and Geothermal Research*, *249*, 123–139. doi: 10.1016/j.jvolgeores.2012.09.002

Garcia, R. F., Klotz, A., Hertzog, A., Martin, R., Grier, S., Kassarian, E., … Mimoun, D. (2022). Infrasound from large earthquakes recorded on a network of balloons in the stratosphere. *Geophysical Research Letters*, *n/a*(n/a), e2022GL098844. Retrieved from `https://agupubs.onlinelibrary.wiley.com/doi/abs/10.1029/2022GL098844` (e2022GL098844 2022GL098844) doi: https://doi.org/10.1029/2022GL098844

Garcia, R. F., Martire, L., Chaigneau, Y., Cadu, A., Mimoun, D., Portus, M. B., … Martin, R. (2020, December). An active source seismo-acoustic experiment using tethered balloons to validate instrument concepts and modelling tools for atmospheric seismology. *Geophysical Journal International*, *225*(1), 186–199. Retrieved from `https://doi.org/10.1093/gji/ggaa589` doi: 10.1093/gji/ggaa589

Gardner, C. S., Hostetler, C. A., & Franke, S. J. (1993). Gravity wave models for the horizontal wave number spectra of atmospheric velocity and density fluctuations. *Journal of Geophysical Research: Atmospheres*, *98*(D1), 1035–1049. doi: 10.1029/92JD02051

Haase, J., Alexander, M. J., Hertzog, A., Kalnajs, L., Deshler, T., Davis, S., … Venel, S. (2018). Around the World in 84 Days. *EOS*. doi: 10.1029/2018eo091907

Hersbach, H., Bell, B., Berrisford, P., Hirahara, S., Horányi, A., Muñoz-Sabater, J., … Thépaut, J.-N. (2020). The ERA5 global reanalysis. *Quarterly Journal of the Royal Meteorological Society*, *146*(730), 1999–2049. doi: 10.1002/qj.3803

Hertzog, A., Cocquerez, P., Guilbon, R., Valdivia, J.-N., Venel, S., Basdevant, C., … Schmitt, É. (2007, December). Stratéole/Vorcore—Long-duration, Superpressure Balloons to Study the Antarctic Lower Stratosphere during the 2005 Winter. *Journal of Atmospheric and Oceanic Technology*, *24*(12), 2048–2061. doi: 10.1175/2007JTECHA948.1

Holasek, R. E., Self, S., & Woods, A. W. (1996). Satellite observations and interpretation of the 1991 mount pinatubo eruption plumes. *Journal of Geophysical Research: Solid Earth*, *101*(B12), 27635-27655. Retrieved from https://agupubs.onlinelibrary.wiley.com/doi/abs/10.1029/96JB01179 doi: https://doi.org/10.1029/96JB01179

Hupe, P., Ceranna, L., Le Pichon, A., Matoza, R. S., & Mialle, P. (2022). International monitoring system infrasound data products for atmospheric studies and civilian applications. *Earth System Science Data Discussions*, *2022*, 1–40. Retrieved from https://essd.copernicus.org/preprints/essd-2021-441/ doi: 10.5194/essd-2021-441

Krishnamoorthy, S., Bowman, D. C., Komjathy, A., Pauken, M. T., & Cutts, J. A. (2020a, October). Origin and mitigation of wind noise on balloon-borne infrasound microbarometers. *The Journal of the Acoustical Society of America*, *148*(4), 2361–2370. doi: 10.1121/10.0002356

Krishnamoorthy, S., Bowman, D. C., Komjathy, A., Pauken, M. T., & Cutts, J. A. (2020b, October). Origin and mitigation of wind noise on balloon-borne infrasound microbarometers. *The Journal of the Acoustical Society of America*, *148*(4), 2361–2370. doi: 10.1121/10.0002356

Krishnamoorthy, S., Lai, V. H., Komjathy, A., Pauken, M. T., Cutts, J. A., Garcia, R. F., … Cadu, A. (2019). Aerial Seismology Using Balloon-Based Barometers. *IEEE Transactions on Geoscience and Remote Sensing*, 1–11. Retrieved from https://ieeexplore.ieee.org/document/8809415/ doi: 10.1109/TGRS.2019.2931831

Marty, J. (2019). The IMS infrasound network: Current status and technological developments. In A. Le Pichon, E. Blanc, & A. Hauchecorne (Eds.), *Infrasound monitoring for atmospheric studies: Challenges in middle atmosphere dynamics and societal benefits* (pp. 3–62). Cham: Springer International Publishing. doi: 10.1007/978-3-319-75140-5_1

Massman, W. J. (1978, September). On the Nature of Vertical Oscillations of Constant Volume Balloons. *Journal of Applied Meteorology*, *17*(9), 1351–1356. doi: 10.1175/1520-0450(1978)017⟨1351:OTNOVO⟩2.0.CO;2

Matoza, R. S., Fee, D., Assink, J. D., Iezzi, A. M., Green, D. N., Kim, K., … Wilson, D. C. (2022). Atmospheric waves and global seismoacoustic observations of the january 2022 hunga eruption, tonga. *Science*, *0*(0), eeeeeeeeeee. Retrieved from https://www.science.org/doi/abs/10.1126/science.abo7063 doi: 10.1126/science.abo7063

Matoza, R. S., Fee, D., Garcés, M. A., Seiner, J. M., Ramón, P. A., & Hedlin, M. a. H. (2009). Infrasonic jet noise from volcanic eruptions. *Geophysical Research Letters*, *36*(8). doi: 10.1029/2008GL036486

Millán, L., Santee, M. L., Lambert, A., Livesey, N. J., Werner, F., Schwartz, M. J., … Froidevaux, L. (2022). The Hunga Tonga-Hunga Ha'apai Hydration of the Stratosphere. *Geophysical Research Letters*, *49*(13), e2022GL099381. doi: 10.1029/2022GL099381

Picone, J. M., Hedin, A. E., Drob, D. P., & Aikin, A. C. (2002). NRLMSISE-00 empirical model of the atmosphere: Statistical comparisons and scientific issues. *Journal of Geophysical Research: Space Physics*, *107*(A12), SIA 15-1-SIA 15-16. doi: 10.1029/2002JA009430

Pierce, A. D., & Posey, J. W. (1971, December). Theory of the Excitation and Propagation of Lamb's Atmospheric Edge Mode from Nuclear Explosions. *Geophysical Journal International*, *26*(1-4), 341–368. doi:

10.1111/j.1365-246X.1971.tb03406.x
Podglajen, A., Hertzog, A., Plougonven, R., & Legras, B. (2016). Lagrangian temperature and vertical velocity fluctuations due to gravity waves in the lower stratosphere. *Geophysical Research Letters*, *43*(7), 3543–3553. doi: 10.1002/2016GL068148
Podglajen, A., Hertzog, A., Plougonven, R., & Žagar, N. (2014). Assessment of the accuracy of (re)analyses in the equatorial lower stratosphere. *Journal of Geophysical Research: Atmospheres*, *119*(19), 11,166–11,188. doi: 10.1002/2014JD021849
Poli, P., & Shapiro, N. M. (2022). Rapid Characterization of Large Volcanic Eruptions: Measuring the Impulse of the Hunga Tonga Ha'apai Explosion From Teleseismic Waves. *Geophysical Research Letters*, *49*(8), e2022GL098123. doi: 10.1029/2022GL098123
Proud, S. R., Prata, A., & Schmauss, S. (2022). The january 2022 eruption of hunga tonga-hunga haapai volcano reached the mesosphere. *Earth and Space Science Open Archive*, 11. Retrieved from `https://doi.org/10.1002/essoar.10511092.1` doi: 10.1002/essoar.10511092.1
Sellitto, P., Podglajen, A., Belhadji, R., Boichu, M., Carboni, E., Cuesta, J., ... Legras, B. (2022). *The unexpected radiative impact of the Hunga Tonga eruption of January 15th, 202.* doi: 10.21203/rs.3.rs-1562573/v1
Vergoz, J., Hupe, P., Listowski, C., Le Pichon, A., Garcés, M. A., Marchetti, E., ... Mialle, P. (2022, August). IMS observations of infrasound and acoustic-gravity waves produced by the January 2022 volcanic eruption of Hunga, Tonga: A global analysis. *Earth and Planetary Science Letters*, *591*, 117639. doi: 10.1016/j.epsl.2022.117639
Vincent, R. A., & Hertzog, A. (2014, April). The response of superpressure balloons to gravity wave motions. *Atmospheric Measurement Techniques*, *7*(4), 1043–1055. doi: 10.5194/amt-7-1043-2014
Watson, L. M., Iezzi, A. M., Toney, L., Maher, S. P., Fee, D., McKee, K., ... Johnson, J. B. (2022, April). Volcano infrasound: Progress and future directions. *Bulletin of Volcanology*, *84*(5), 44. doi: 10.1007/s00445-022-01544-w
Waxler, R., & Assink, J. (2019). Propagation Modeling Through Realistic Atmosphere and Benchmarking. In A. Le Pichon, E. Blanc, & A. Hauchecorne (Eds.), *Infrasound Monitoring for Atmospheric Studies: Challenges in Middle Atmosphere Dynamics and Societal Benefits* (pp. 509–549). Cham: Springer International Publishing. doi: 10.1007/978-3-319-75140-5_15
Waxler, R., Hetzer, C., Assink, J., & Velea, D. (2021, September). *Chetzer-ncpa/ncpaprop-release: NCPAprop v2.1.0.* Zenodo. doi: 10.5281/zenodo.5562713
Woulff, G., & McGetchin, T. R. (1976, June). Acoustic Noise from Volcanoes: Theory and Experiment. *Geophysical Journal International*, *45*(3), 601–616. doi: 10.1111/j.1365-246X.1976.tb06913.x
Wright, C. J., Hindley, N. P., Alexander, M. J., Barlow, M., Hoffmann, L., Mitchell, C. N., ... Yue, J. (2022, June). Surface-to-space atmospheric waves from Hunga Tonga-Hunga Ha'apai eruption. *Nature*, 1–3. doi: 10.1038/s41586-022-05012-5
Young, E. F., Bowman, D. C., Lees, J. M., Klein, V., Arrowsmith, S. J., & Ballard, C. (2018, May). Explosion-Generated Infrasound Recorded on Ground and Airborne Microbarometers at Regional Distances. *Seismological Research Letters*, *89*(4), 1497–1506. doi: 10.1785/0220180038
Yuen, D. A., Scruggs, M. A., Spera, F. J., Zheng, Y., Hu, H., McNutt, S. R., ... Tanioka, Y. (2022, March). Under the Surface: Pressure-Induced Planetary-Scale Waves, Volcanic Lightning, and Gaseous Clouds Caused by the Submarine Eruption of Hunga Tonga-Hunga Ha'apai Volcano Provide an Excellent Research Opportunity. *Earthquake Research Advances*, 100134. doi:

10.1016/j.eqrea.2022.100134

Supporting Information for "Stratospheric balloon observations of infrasound waves from the January 15 2022 eruption of the Hunga volcano, Tonga"

Aurélien Podglajen[1], Alexis Le Pichon[2], Raphaël F. Garcia[3], Solène Gérier[3],

Christophe Millet[2], Kristopher Bedka[4], Konstantin Khlopenkov[5], Sergey

Khaykin[6], Albert Hertzog[7]

[1]Laboratoire de Météorologie Dynamique (LMD/IPSL), École polytechnique, Institut polytechnique de Paris, Sorbonne Université,

École normale supérieure, PSL Research University, CNRS, Paris, France

[2]CEA, DAM, DIF, 91297 Arpajon, France

[3]Institut Supérieur de l'Aéronautique et de l'Espace (ISAE-SUPAERO), Université de Toulouse, 10 Ave E. Belin 31400 Toulouse,

France

[4]NASA Langley Research Center, Hampton, Virginia, USA

[5]Science Systems and Applications, Inc., Hampton, Virginia, USA

[6]Laboratoire Atmosphères, Observations Spatiales (LATMOS), UVSQ, Sorbonne Université, CNRS, IPSL, Guyancourt, France

[7]Laboratoire de Météorologie Dynamique (LMD/IPSL), Sorbonne Universit, École polytechnique, Institut polytechnique de Paris,

École normale supérieure, PSL Research University, CNRS, Paris, France

Contents of this file

---

2. Figures S1 to S2

Introduction

This supplementary information contains a description of the effects of the correction to raw pressure data (Equation (1) of the paper) (S1), a description of the methodology used to derive stereoscopic cloud top height in the HT-HH plume from Himawari-8 and GOES-17 brightness temperature data (S2), details on infrasound travel speed estimations (S3) and a comparison of background pressure variability between balloon STR1 and ground station IS22 (S4).

Text S1.

As mentioned in Sect. 2.1 of the paper, we attempt to correct for the effect of vertical motion of the balloon in the hydrostatic pressure gradient

$$p = p_l \exp\left(\frac{g}{R_d T}\zeta'\right) - \overline{p} \tag{1}$$

where p_l is the raw (balloon-following) pressure and p the Eulerian pressure which would be measured in the absence of altitude variations. Without a high-frequency inertial measurement unit (IMU) onboard, 30-s vertical GPS position has to be interpolated at 1 s to compute ζ'. The raw pressure and Eulerian (corrected) pressure spectra are shown in Fig. S1. The correction effectively cancels out balloon neutral oscillations and affects the spectra up to ~17 mHz (half the sampling frequency of ζ'). It is likely that hydrostatic pressure flucatuations are still impacting data above that frequency, but the temporal resolution of the altitude dataset does not enable us to account for that effect. We anticipate that an IMU would enable to extend the range to both lower and higher frequencies. Fortunately, the power spectral density of altitude fluctuations drops sharply above the balloon oscillation frequency (e.g., Podglajen et al., 2016), so that the correction becomes unnecessary as its spectrum likely falls below geophysical pressure signals such as the oceanic microbarom, and infrasound from the Hunga eruption or eathquakes.

Besides sampling frequency, another limiting factor is the precision of GPS data, which induces a noise floor in the correction. Our estimates however puts this noise floor either below or at the level of observed background pressure fluctuations, making the correction useful. A last limiting factor which is not well-constrained in our analysis is the lag between pressure and position measurements. We tried to account for this small time shift (a few hundreds of ms), but it may be variable, which would result in an imperfect cancellation of motions around the balloon oscillations (as might be suspected from Fig. S1). Hence, no conclusion can be drawn regarding the actual atmospheric variability near the frequency of balloon oscillation.

Nevertheless, for the purpose of our study, the correction performs well enough (Fig. S1) and is essentially cosmetic, since it does not affect the infrasound range above 20 mHz. Yet, it enables us to more clearly identify the isolated bump related to Hunga infrasound, which otherwise sometimes remains merged with that of the balloon oscillations.

Text S2.

Two primary steps were used in the derivation of cloud top height for the Hunga eruption cloud based on GOES-17 and Himawari-8 geostationary satellite observations: 1) spatially matching simultaneous observations from the two satellites, and 2) using the stereoscopy principle to construct a 3D profile of the cloud. Because the two satellites have sufficiently different viewing angles, then it can be possible to derive a cloud top height with accuracy equal to or better than the spatial resolution of the imagery being used. Level 1B infrared (IR) brightness temperature (BT) data in the 10.3 μm is collected at 2 km/pixel nadir resolution and nearly simultaneously from GOES-17 and Himawari-8 because the imagers on these satellites, the Advanced Baseline Imager (ABI) and Advanced Himawari Imager (AHI) respectively, are nearly identical and have the same scan initiation times and scan rate. Although IR imagery is of lower resolution than the visible, it has its own advantages as it is free of shadows, is nearly isotropic, and is available at nighttime. Pixel geolocation in Level 1B data is obtained by intersecting the instant view axis of the imager instrument with the Earth reference ellipsoid, and thus the nominal image registration is accomplished assuming a zero elevation of observed scenes. Once these Level 1B data are reprojected from satellites pixel/line space to a geographical projection, any elevated scene exhibits a parallax displacement, which is different for images recorded at different viewing angles. With simple geometric transformations, the two parallax displacements from the two satellites can be directly related to the sought height. An algorithm developed at NASA Langley Research Center uses image subsets (chips) ranging from 8x8 to 20x20 pixel sizes to obtain a cross correlation between chips from the two image sources. Trying different relative displacements between the chips consecutively yields the highest correlation at the position of optimal displacement, which corresponds to the actual height for that image subset. Analyses indicate that we were able to achieve a subpixel accuracy when calculating the position of the highest correlation. This translates to a typical accuracy of the derived height on the order of 0.2-0.4 km. When the analyzed image chips have little texture, the correlation matching may fail for smaller chip sizes. In that case, a larger chip can be used to obtain a reliable peak in the correlation profile, but that lowers the effective resolution of the resulting map of retrieved heights. More than 90% of image chips, however, were reliably matched using the 8x8 chip size, which helps to resolve smaller features and details within the eruption cloud, like the small peaks of cloud extending above 50 km altitude. Overall, we estimate the spatial resolution of the cloud top height retrieval product to be ~4-6 km/pixel. This algorithm was applied to satellite data from 0400 to 2350 UTC on 15 January 2022 to quantify heights reached by the eruption cloud and document its temporal evolution.

Text S3.

To crudely estimate average propagation speed from Hunga to the receivers, we take advantage of the good visual correlation between the signals at balloon STR1 and stations IS22, IS07, IS36 and IS40 and cross-correlate time series of 3-minute 30-40 mHz-filtered signal variance between the reference station IS22 and the other records. The optimal lag Δt corresponding to maximum correlation is interpreted as caused by the difference in travel time between Hunga and the two sensors, i.e.:

$$\Delta t = \frac{d_s}{c_s} - \frac{d_{IS22}}{c_{IS22}} \tag{2}$$

where d_s is the sensor's range, d_{IS22} the range at IS22, c_{IS22} the average group velocity from Hunga to IS22, and c_s the average group velocity from Hunga to sensor. Without any prior knowledge of the event chronology or infrasound propagation speed, we cannot however anchor c_s which remains relative to c_{IS22}. To circumvent this issue, we assume that, range excluded, propagation properties are similar between IS22 and IS07. This is based on the premise that IS22 approximately lies on the orthodrome from Hunga to IS07 and that atmospheric conditions are relatively homogeneous along that path (see Fig. 1 a)), Note, however, that the lower boundary condition varies (from ocean to Australian land). Since we are interested in fitting the arrival times, or onsets, more than the position of the maxima, the lag-correlation is performed on decimal logarithm after setting values around the noise level of the sensor to zero. This manages sufficiently well to capture speed for short-range receivers, but fails where dispersion has important effect, such as at TTL4 with obvious double arrivals for WP1 and WP3. Hence, provided values are only indicative.

Finally, note that special care has to be taken with the balloons which are drifting during the day, affecting distance estimates. In order to account for that effect and since we are interested in average ground-relative propagation speeds, we first computed an approximate arrival time using a nominal propagation speed of 275 m/s. Then, the distance corresponding to the period of the arrivals was selected for a more precise estimate of distance and travel speed. Finally, reduced time

$$t_r = t - \frac{d(t)}{c_s} \tag{3}$$

used in Figure 4 is computed using the time-dependent range.

Text S4.

Figure S2 presents a comparison of background pressure power levels between ground station IS22 and balloon STR1 from January 16 00:00 UTC until 14:00 UTC (a period without any arrival from Hunga waves). This period includes some daytime at IS22 with increased noise levels due to turbulences and some nighttime with lower noise levels (see

Fig. 3 of the paper). Both average noise levels and 2nd and 98th quantile are shown to provide a sense of the different conditions encountered (weak vs large noise).

The background recorded on the balloons is clearly below what is observed on average at the ground (left panel), and mean balloon background only compares with the lowest values seen at IS22. This difference tends to increase towards higher frequencies. These statements concern raw pressure, but as we saw from PE calculations (Fig. 1 c)-e)) and the first overpasses (Fig. 4 b), scaled pressure is a more constant quantity and better suited for ground versus upper-air signal-to-noise ratio comparison in the Hunga case. Accounting for this effect and multiplying the balloon noise PSD by the scaling factor $\frac{\rho_{IS22}}{\rho_{STR1}}$, it becomes more comparable to that from ground receivers (right panel). In the infrasound range up to the 0.1 Hz (just below the microbarom peak at 0.2 Hz), weak noise conditions at the ground seem associated with a larger SNR at IS22 than in balloon data. However, both above that frequency and in strong noise conditions, there seems to be a significant advantage of upper-air measurements.

References

Podglajen, A., Hertzog, A., Plougonven, R., & Legras, B. (2016). Lagrangian temperature and vertical velocity fluctuations due to gravity waves in the lower stratosphere. *Geophysical Research Letters*, *43*(7), 3543–3553. doi: 10.1002/2016GL068148

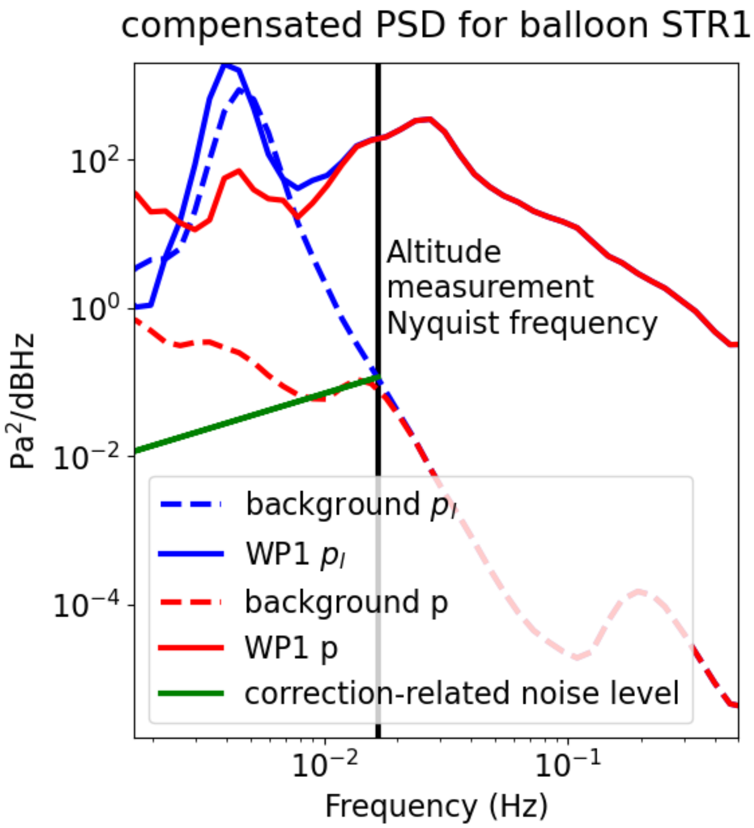

Figure S1. Compensated power spectral density of balloon STR1 raw pressure data p_l and pressure data p corrected for vertical oscillations using Eq. (1), during the overpass of WP1 and a background pre-eruption period. The impact of limited temporal resolution and precision of altitude measurements is illustrated by the black lines, which show the corresponding Nyquist frequency and estimated induced noise level.

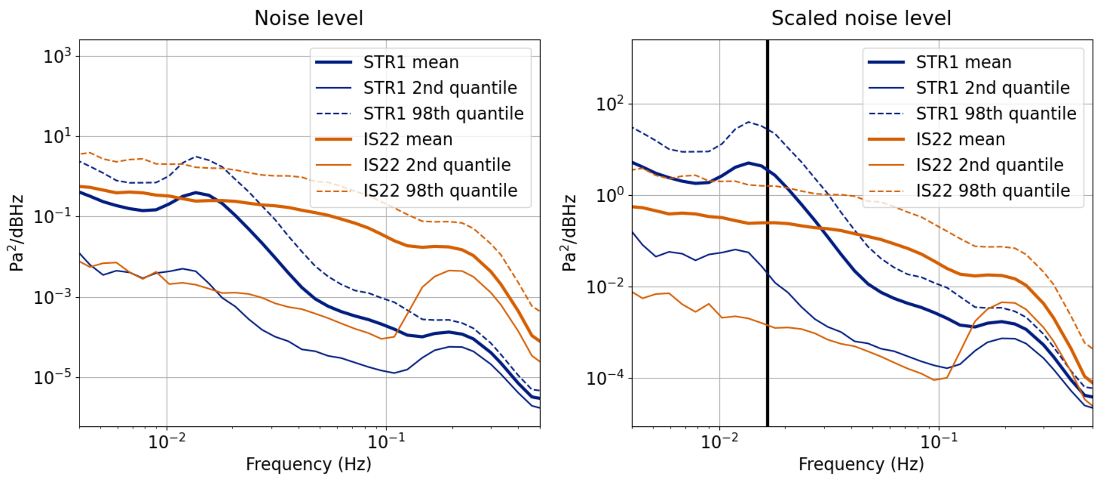

Figure S2. (Left) Compensated power spectral density of background pressure variability recorded ("noise") by IS22 and STR1 from Jan. 16 00:00 UTC to Jan. 16 14:00 UTC. (right panel) Same as left, but the balloon background signal is scaled by $\frac{\rho_s}{\rho_b}$, to mirror a signal-to-noise ratio by accounting for infrasound signal decrease (i.e. relative increase of noise) with decreasing ambient density.